

CHAPTER 3
RESULTS AND DISCUSSION

3.1 Synthesis of TiO₂ by thermal hydrolysis

3.1.1 Crystal Structure and BET specific surface area

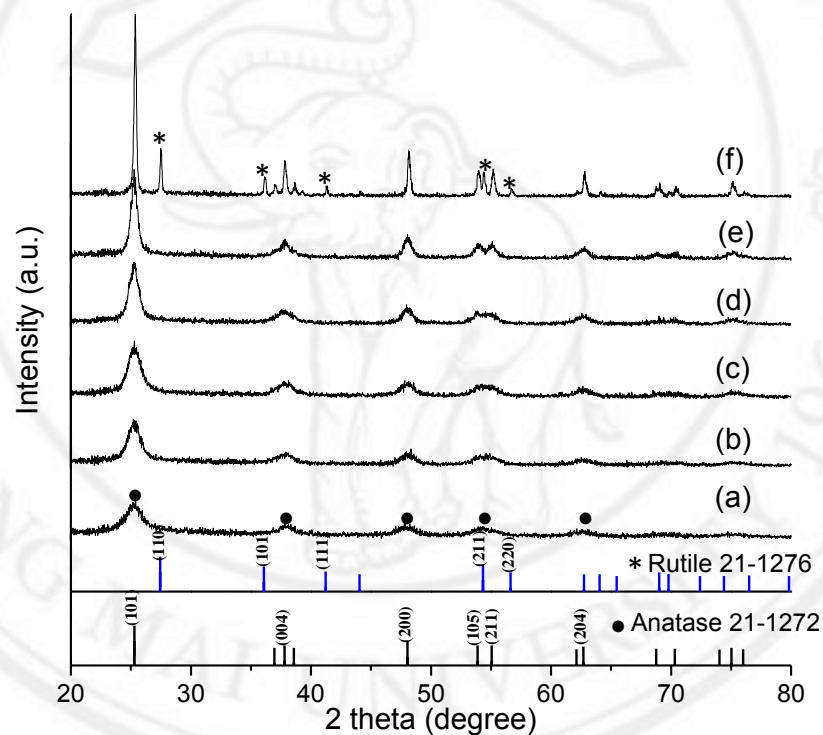
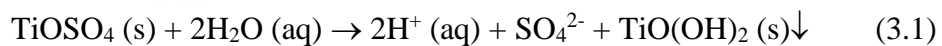


Figure 3.1 X-ray diffraction patterns of (a) as-prepared TiO₂ and TiO₂ calcined at (b) 300, (c) 400, (d) 500, (e) 600 and (f) 900 °C

In the present study, TiO₂ was simply prepared by thermal hydrolysis of TiOSO₄. The hydrolysis of TiOSO₄ results in the formation of white precipitate (TiO(OH)₂) according to the following equation 3.1 [1]:



The sample was then dried at 60 °C and calcined at different temperatures. XRD patterns of the as-prepared and the calcined powders are shown in Figure 3.1. Results indicated that the as-prepared powder was already in the form of anatase TiO₂. The peaks at 25.37, 37.83, 48.15, 54.13 and 62.89° corresponded to the (101), (004), (200), (105) and (204) planes of anatase (JCPDS file no. 21-1272). Upon calcination of the sample in the range of 300-600 °C (Fig 3.1 (b)-(e)), the increase of diffraction peak intensity was observed, indicating enhanced crystallinity of the anatase phase. The sample remained in the form of pure anatase up to 800 °C (data not shown) and partially transformed into rutile phase at 900 °C (Figure 3.1 (f)). The peaks at 27.52, 36.14, 41.37, 54.43, 56.72 and 62.81° corresponded to the (110), (101), (111), (211), (220) and (002) planes of rutile with JCPDS file no. 21-1276. Broad diffraction peaks observed from the TiO₂ calcined at low temperature indicated the presence of crystalline particles with small size, whereas sharp diffraction peaks, indicating large crystalline particle size, were found from the sample calcined at high temperature. The high thermal treatment also induced anatase to rutile phase transformation and caused the reduction in specific surface area as reported in Table 3.1. Table 3.1 presented the calculated phase composition and crystallite sizes of the TiO₂ calcined at different temperatures are presented. The anatase and rutile crystallite sizes (D in nm) were determined by applying the Scherrer equation on the (101) and the (110) diffraction peaks, respectively[2]. According to Table 3.1, increasing the calcination temperature from 300 to 600 °C resulted in enhanced anatase crystallite size from 4.5 to 11.9 nm. Increasing the temperature further to 900 °C produced the mixed phase of 75 wt.% anatase and 25 wt.% rutile with the anatase and rutile crystallite sizes of 34.9 and 38.3 nm, respectively. The increase of crystal

size upon high thermal treatment also accompanied with a significant decrease of BET specific surface area as reported in Table 3.1. As the calcination temperature was increased from 300 to 900 °C, the specific surface area drastically decreased from 169.38 to 25.46 m²/g.

Table 3.1 Phase content and crystallite size of TiO₂ nanoparticles obtained from different calcination temperatures

Calcination temperature (°C)	Amount of each phase (wt.%)		Crystallite size (nm)		Specific surface area (m ² /g)
	Anatase	Rutile	Anatase	Rutile (110)	
			(101) plane	plane	
As-prepared	100	–	4.5	–	211.05
300	100	–	5.3	–	169.38
400	100	–	6.0	–	123.38
500	100	–	7.7	–	85.99
600	100	–	11.9	–	60.97
900	75.4	24.6	34.9	38.3	25.46

3.1.2 Morphology of TiO₂

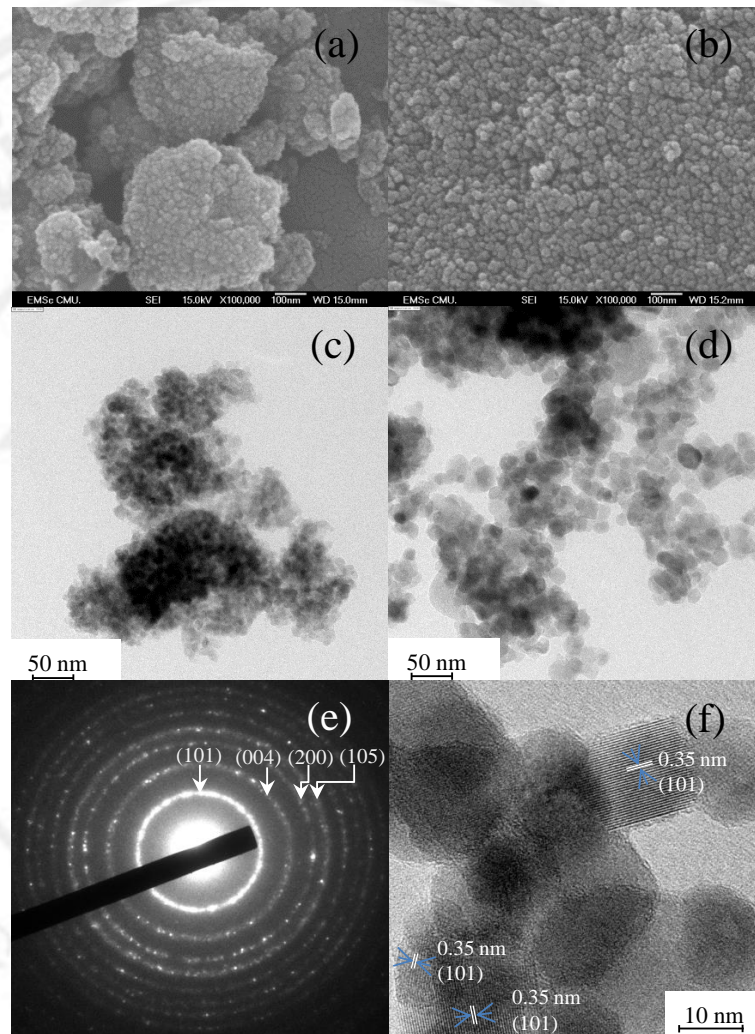


Figure 3.2 SEM and TEM micrographs of TiO₂ calcined at 300 °C (a, c) and 600 °C (b, d) respectively, and the HRTEM image (f) and SAED pattern (e) of TiO₂ calcined at 600 °C

The SEM micrographs of TiO₂ calcined at 300 and 600 °C given in Figure 3.2 (a) and (b) respectively, showed that TiO₂ secondary particles were comprised of agglomerated irregular primary particles. The size of the primary particles observed from the TEM images (Figure 3.2 (c) and (d)) depended on the calcination temperature. The crystallite size was 8-10 nm at 300 °C (Figure 3.2 (c)). As the

temperature of calcination was raised to 600 °C, the crystallite size increased to 16-22 nm (Figure 3.2 (d)). The corresponding selected area electron diffraction (SAED) pattern of Figure 3.2 (e) showed discontinuous diffraction rings, indicating that the sample was polycrystalline. The ring can be indexed as (101), (004), (200) and (105) of anatase TiO₂ which was in accordance with the XRD results. High resolution TEM image showing lattice fringes of the TiO₂ calcined at 600 °C (Figure 3.2 (f)) revealed the crystalline nature of the particles. The spacing between the two adjacent lattice planes was 0.35 nm, corresponding to the *d*-value for anatase (101) plane.

3.1.3 FTIR results of TiO₂

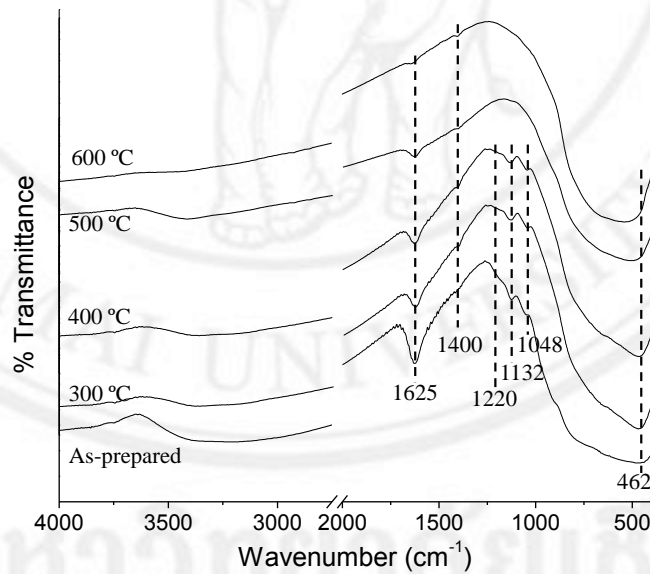


Figure 3.3 IR spectra of as-prepared TiO₂ and the TiO₂ calcined at different temperatures.

The IR spectra of as-prepared TiO₂ and TiO₂ calcined at different temperatures (300-600 °C) are presented in Figure 3.3. The peak at 462 cm⁻¹ in the range of 400-1000 cm⁻¹ was a contribution from the anatase TiO₂ [3]. The broad peak in the range of 3000-3600 cm⁻¹ and the peak at 1625 cm⁻¹ corresponded to the bending vibrations of physisorbed H₂O and surface hydroxyl groups [4]. Small IR peak at 1400 cm⁻¹ due to the deformation vibration of adsorbed ammonia was also observed in the obtained samples. Three IR absorption peaks at 1220, 1132 and 1048 cm⁻¹ assigned to the stretching vibration of SO₄²⁻ ions coordinated to the surface Ti⁴⁺ ions [5] were found from the TiO₂ calcined upto 400 °C. However, these peaks disappeared when the calcination temperature was above 500 °C, indicating no contamination from the sulfate species. The IR results suggested that trace amount of sulfate ions is hardly removed, therefore high temperature treatment or good washing of the particles are necessary.

3.1.4 UV-vis diffuse reflectance spectra of TiO₂ and its application as a photocatalyst

UV-vis diffuse reflectance spectroscopy has been used to investigate the optical properties of the synthesized samples compared with that of the commercial TiO₂ P25. The optical absorption spectra of the samples shown in Fig. 4 (a) were converted from diffuse reflectance spectra using the Kubelka-Munk (K-M) formula [6]:

$$F(R_{\infty}) = \frac{K}{S} = \frac{(1-R_{\infty})^2}{2R_{\infty}} \quad (3.2)$$

where R_{∞} is the absolute diffuse reflectance for an infinitely thick sample, K and S are the sample absorption and scattering coefficients, respectively. According to

Figure 3.4 (a), the commercial TiO₂ P25 had an absorption onset at 382 nm while the TiO₂ calcined at 300 °C and 600 °C had the absorption edges at 385 and 390 nm, respectively. To determine band gap energies of the samples, the Tauc equation, which relates the absorption edge, the energy of incident photons and the band gap (E_g) of a semiconductor sample as shown below, has been employed [7].

$$\alpha h\nu = A(h\nu - E_g)^n \quad (3.3)$$

where A is a proportionality constant, $h\nu$ is the photon energy and α is the extinction coefficient which is proportional to $F(R_\infty)$. The value of n depends on the interband transition mechanism of the material. For TiO₂, the n value of 2 for an indirect allowed transition has been applied [8], [9]. Therefore, the Tauc equation becomes

$$F(R_\infty)h\nu = A(h\nu - E_g)^2 \quad (3.4)$$

By plotting $(F(R_\infty)h\nu)^{1/2}$ versus $h\nu$, the band gap energy can be determined by linear extrapolation to the energy axis as shown in Fig. 3.4 (b). The band gap values of the TiO₂ P25 and the TiO₂ calcined at 300 and 600°C were 3.27, 3.30 and 3.21 eV, respectively. Although the three samples possessed similar band gap energies, their light absorbance presented in Fig. 3.4 (b) were significant different. The lowest and highest absorption intensities were observed from TiO₂ P25 and the TiO₂ calcined at 600 °C, respectively. Although the three samples possessed no significant differences in band gap energies, their light absorbance (Fig.3.4(a)) obviously differed from each other. The TiO₂ calcined at 300 and 600 °C showed remarkably enhanced UV light absorption intensity compared with that of the commercial TiO₂. The different absorption intensity was ascribed to the differences in various intrinsic properties such as particle size, surface area and sample crystallinity[10]. The strong light absorbance

observed in Fig. 3.4(a) would be beneficial to the photogeneration of electron–hole pair charge carriers and the improvement of the photocatalytic performance.

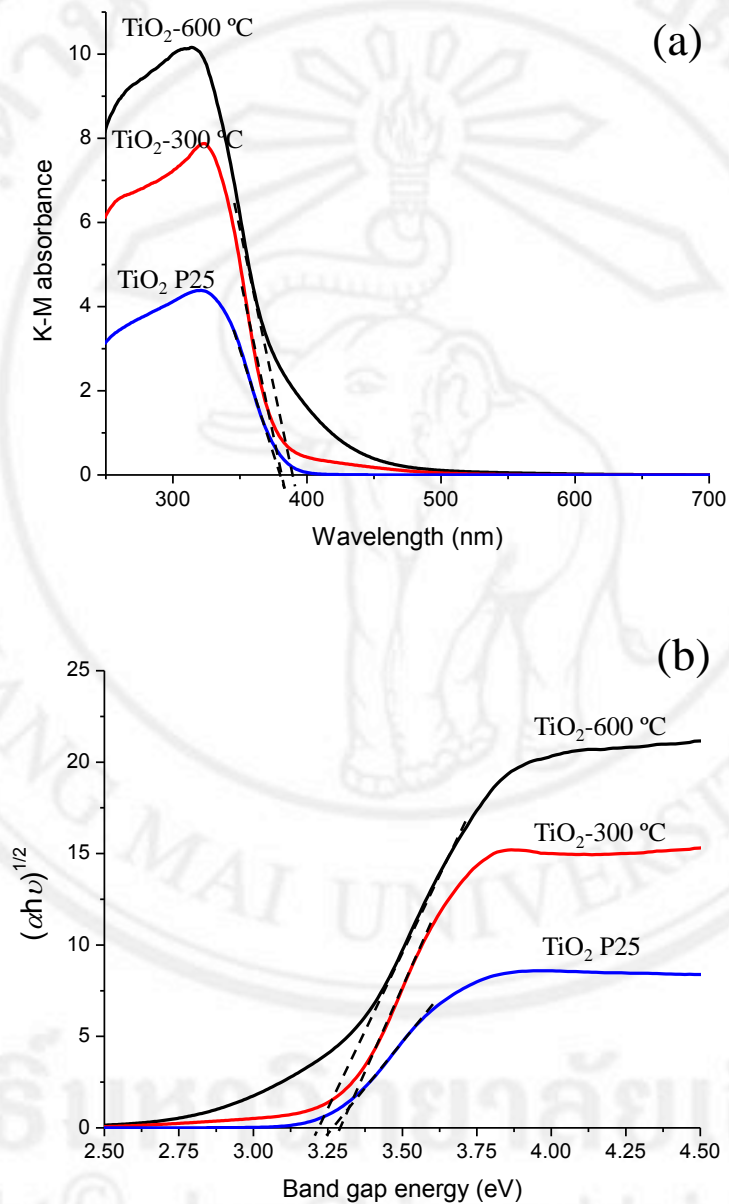


Figure 3.4 (a) Kubelka-Munk absorbance plot and (b) absorption plot for the indirect semiconductor transitions vs. energy of the band gap.

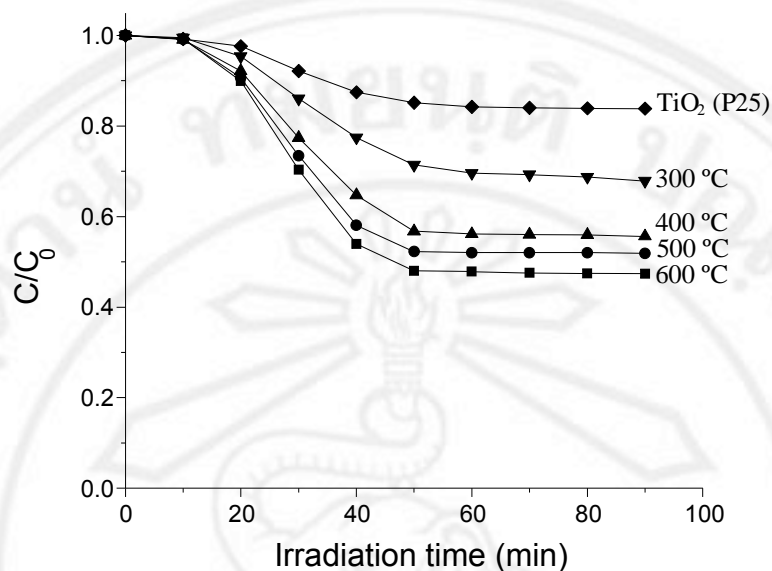


Figure 3.5 Photocatalytic mineralization of phenol under UV light irradiation by TiO₂ calcined at 300 (▼), 400 (▲), 500 (●) and 600 °C (■) compared with that by the commercial TiO₂ P25 (◆).

Fig. 3.5 showed photocatalytic activities of the TiO₂ calcined at 300 and 600 °C evaluated by the mineralization of phenol under UV irradiation. For comparison, the photocatalytic activity of the commercial TiO₂ P25 was also determined under an identical condition. The TiO₂ calcined at 600 °C gave the highest photoactivity of *ca.* 52.5 % whereas the one calcined at 300 °C and TiO₂ P25 provided only *ca.* 31.0% and 16 %, respectively. The results clearly demonstrated the superior performances of the TiO₂ synthesized in this study compared with the commercial P25 catalyst. Although the TiO₂ calcined at 300 °C had the highest surface area of 169 m²/g compared with that of P25 (50 m²/g) and of TiO₂ calcined at 600 °C (61 m²/g), this material did not provide the best photoactivity. Therefore, the surface area is unlikely the main factor affecting the photocatalytic activity observed in this study. Since the band gap

energies of the three samples are nearly the same, therefore the light absorption intensity might be the important factor responsible for the observed photocatalytic performances. Enhanced light absorption intensity was previously reported to be beneficial to photoactivity of the material as more electron-hole pairs being generated in the photocatalytic process [11]. Therefore, the high photocatalytic activity of the TiO_2 calcined at 600 °C in this study was attributed to the great light absorption intensity of the material.

3.2 Characterization of Carboxylic acid-modified TiO_2 and its application as a photocatalyst

3.2.1 Crystal Structure and BET specific surface area

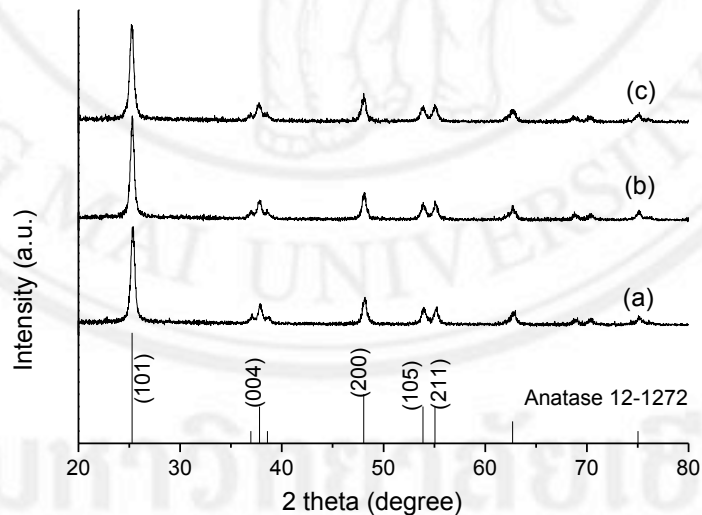


Figure 3.6 X-ray diffraction patterns of TiO_2 :CA in (a) 1:0.5, (b) 1:1 and (c) 1:2 mole ratios calcined at 600 °C for 3h.

The phase composition and the crystallite size of carboxylic acid modified TiO_2 samples were evaluated by X-ray diffraction analysis. Figure 3.6 presents XRD

pattern of Cinnamic acid-modified TiO₂ at different molar ratios of 1:0.5, 1:1 and 1:2 (a-c) respectively. All samples have been calcined at 600 °C for 3h. The peaks at 25.37, 37.83, 48.15, 54.13 and 62.89° corresponded to the (101), (004), (200), (105) and (204) planes of anatase (JCPDS file no. 21-1272). The phase composition of TiO₂ modified by cinnamic acid (CA) was not changed in comparison with the unmodified TiO₂ at the same condition and the TiO₂ modified by cinnamic acid (CA) provided the crystallite size compared with unmodified TiO₂.

Phase composition, crystallite sizes and specific surface area of carboxylic acid-modified TiO₂ nanoparticles calcined at different temperature are presented in Table 3.2. The crystal size of carboxylic acid-modified TiO₂ was estimated according to the Scherrer's equation [2]. It was found that increasing the mole ratio of cinnamic acid: Ti resulted in the enhancement of specific surface area of the samples, however no significant difference in terms of particle size was observed upon increasing the acid amount. Table 3.2 also suggested that the TiO₂ modified by benzoic acid (BA) provided the highest surface area compared with that from salicylic acid (SA) and cinnamic acid (CA). The increased surface area upon acid modification was ascribed to the presence of nonpolar group-containing carboxylic acids which was beneficial to the formation of small-sized and narrow size-distributed anatase TiO₂ nanoparticles [12].

Table 3.2 Phase composition, crystallite size and specific surface area of acid-modified TiO₂ nanoparticles

Samples	Amount of each phase (wt.%)		Crystallite size (nm)		Specific surface area (m ² /g)
	Anatase	Rutile	Anatase (101) plane	Rutile (110) plane	
Calcined 600 °C 3h					
TiO ₂ :CA1:0.5	100	–	20	–	65.34
TiO ₂ :CA 1:1	100	–	23	–	71.59
TiO ₂ :CA 1:2	100	–	24	–	78.21
TiO ₂ :BA 1:1	100	–	19	–	85.26
TiO ₂ :SA 1:1	100	–	20	–	82.78

3.2.2 morphology of acid-modified TiO₂

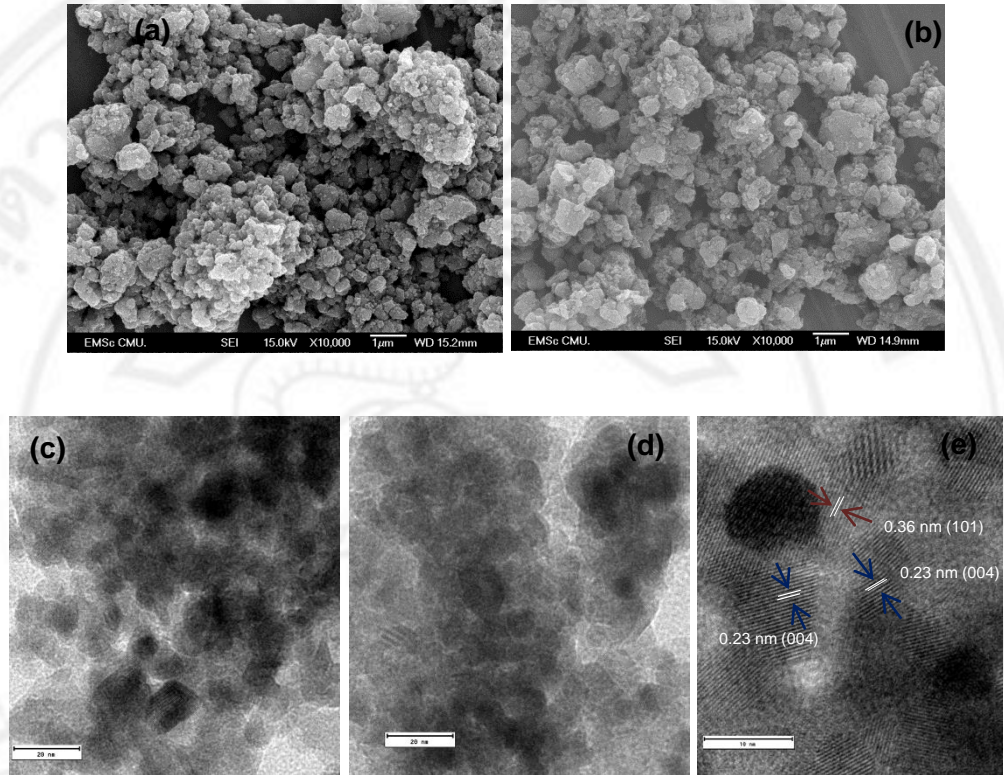


Figure 3.7 SEM and TEM micrographs of TiO₂:CA in 1:0.5 (a, c) and 1:1 (b, d) mole ratios calcined at 400 °C respectively, and SAED pattern (e) of TiO₂:CA in ratio 1:1 calcined at 400 °C.

Figure 3.7 (a,b) presents the SEM images of TiO₂:CA in 1:0.5 and 1:1 mole ratio, respectively. The results showed that CA-modified TiO₂ secondary particles were comprised of agglomerated irregular primary particles. The average particle sizes observed from the TEM images of TiO₂:CA in 1:0.5 (c) and 1:1 (d) mole ratios were 6-20 nm. Results suggested that the loading amount of CA has no significant effect on the particle size. High resolution TEM image (Fig. 3.7 (e)) showing lattice fringes of the TiO₂:CA in 1:1 mole ratio revealed the crystalline nature of the

particles. The spacing between the two adjacent lattice planes were 0.23 and 0.36 nm, corresponding to the d -values for anatase (004) and (101) plane respectively.

3.2.3 FTIR results of acid-modified TiO₂

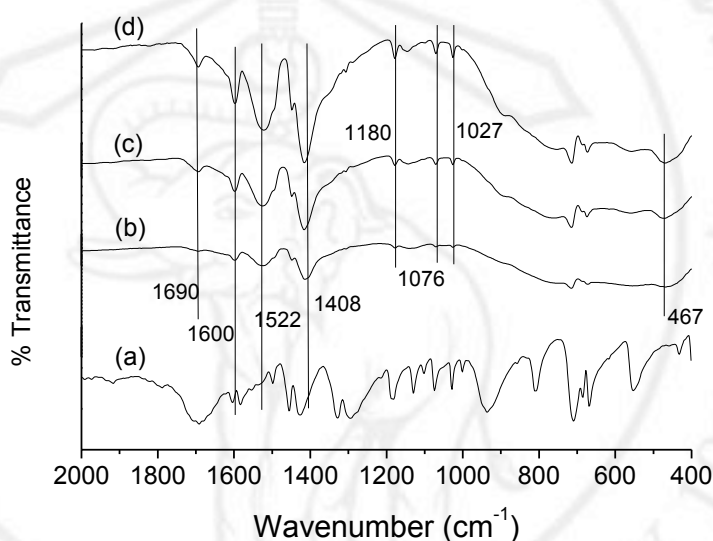
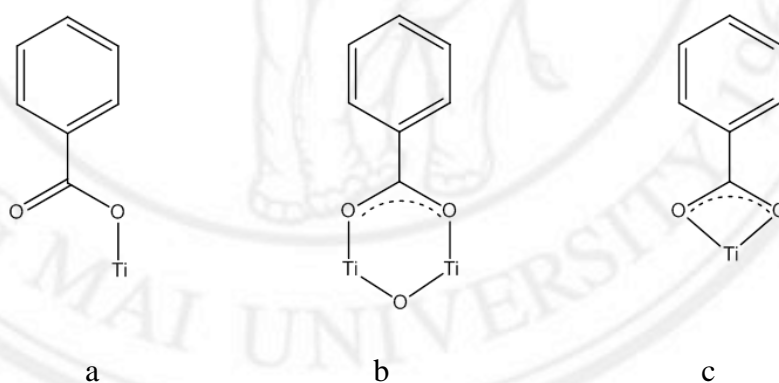


Figure 3.8 IR spectra of (a) BA and as-prepared TiO₂:BA in (b) 1:0.5, (c) 1:1 and (d) 1:2 mole ratios

FT-IR spectra of BA and as-prepared TiO₂ modified with BA in different mole ratios are shown in Figure 3.8 (a-d). In the spectrum of BA (Figure 3.8a), the absorption bands are attributed to the stretching and bending coupled C-OH vibrations ($\nu_{\text{C-OH}}$, at 1320-1280 cm⁻¹) [13], the in-plane bending of O-H ($\delta_{\text{O-H}}$, at 1430 cm⁻¹), and the stretching band of the carboxylic acid ($\nu_{\text{C=O}}$, at 1690 cm⁻¹) while the bands at 1601 and 1453 cm⁻¹ are due to C-C/C=C stretching vibration of phenyl ring ($\nu_{\text{C=C}}$) [13]. The spectra of as-prepared TiO₂:BA at different mole ratios (Figure 3.8 (b-d)) exhibited the $\nu_{\text{C=C}}$ band at 1600 cm⁻¹, the $\nu_{\text{C=O}}$ stretching vibration of carboxylic acid

at 1680 cm^{-1} . The peaks of asymmetric (ν_{as} , at 1522 cm^{-1}) and symmetric (ν_s , at 1408 cm^{-1}) stretching vibrations of carboxylate anion (COO^-) due to the splitting of carboxylate groups complexed with surface Ti centers [14] were also observed. The band at 467 cm^{-1} was a contribution from the anatase TiO_2 [3]. The binding form of carboxylic acids on the TiO_2 nanoparticles (Scheme 1) can be characterized by the separation ($\Delta\nu_{a-s}$) between ν_{as} and ν_s of carboxylate anion (COO^-). Generally, the band separation of $350\text{-}500\text{ cm}^{-1}$, $150\text{-}180\text{ cm}^{-1}$ and below 140 cm^{-1} are for monodentate binding, bidentate bridging and bidentate chelating. In the case of BA-modified TiO_2 (Figure 3.7), the $\Delta\nu_{a-s}$ value of 114 cm^{-1} implies a bidentate chelating form.



Scheme 1. Possible binding modes of COOH group on TiO_2 Nanoparticles:

monodentate binding (a), bidentate bridging (b) and bidentate chelating [13].

For comparison, FT-IR spectra of cinnamic acid and as-prepared TiO_2 modified with cinnamic acid (CA) at different mole ratio are shown in Figure 3.9 (a-d). In the spectrum of CA (Figure 3.9a), the bands are attributed to the stretching and bending coupled C-OH vibrations ($\nu_{\text{C-OH}}$, at $1320\text{-}1280\text{ cm}^{-1}$) [13], the in-plane

bending of O-H ($\delta_{\text{O-H}}$, at 1430 cm^{-1}), and the stretching band of the carboxylic acid ($\nu_{\text{C=O}}$, at 1690 cm^{-1}) while the band at 1636 and 1450 cm^{-1} is due to the C-C/C=C stretching vibration of phenyl ring ($\nu_{\text{C=C}}$) [13]. In the spectra of as-prepared $\text{TiO}_2:\text{CA}$ at different molar ratio Figure 3.9 (b-d) exhibit the $\nu_{\text{C=C}}$ band at 1636 cm^{-1} , the $\nu_{\text{C=O}}$ stretching vibration of carboxylic acid at 1680 cm^{-1} , the peak at 467 cm^{-1} was a contribution from the anatase TiO_2 [3] as well as the carboxylate anion (COO^-) asymmetric (ν_{as} , at 1513 cm^{-1}) and symmetric (ν_{s} , at 1404 cm^{-1}) stretching bands due to the splitting of carboxylate groups complexed with surface Ti centers[14]. The value of $\Delta\nu_{\text{a-s}} = 109$ of $\text{TiO}_2:\text{CA}$ at different mole ratio implies a bidentate chelating form.

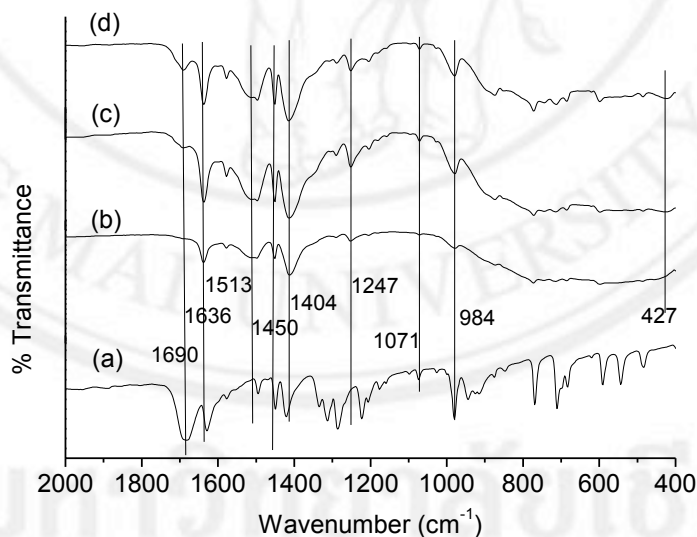


Figure 3.9 IR spectra of (a) Cinnamic acid and as-prepared $\text{TiO}_2:\text{CA}$ in (b) 1:0.5, (c) 1:1 and (d) 1:2 mole ratios

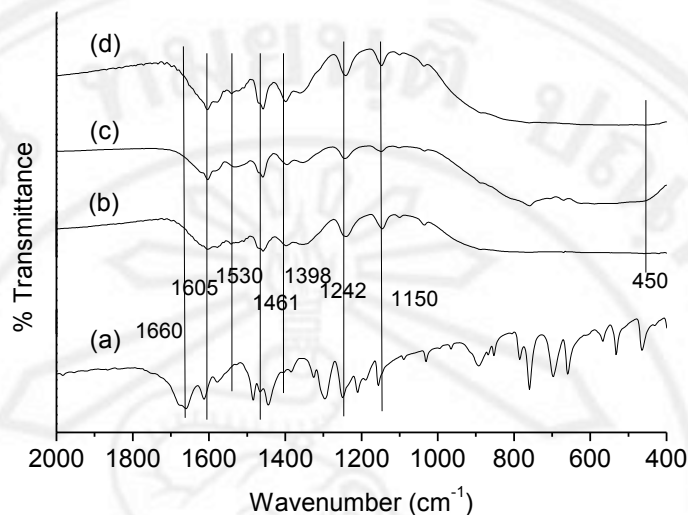
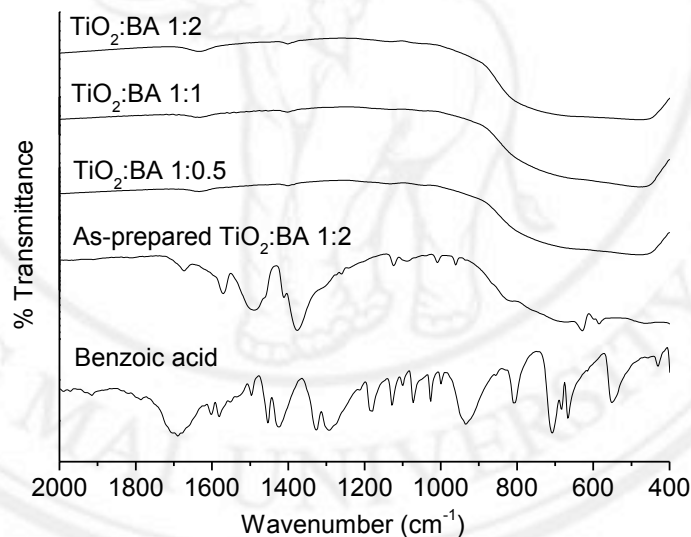


Figure 3.10 IR spectra of (a) Salicylic acid and as-prepared TiO_2 :SA in (b) 1:0.5, (c) 1:1 and (d) 1:2 mole ratios

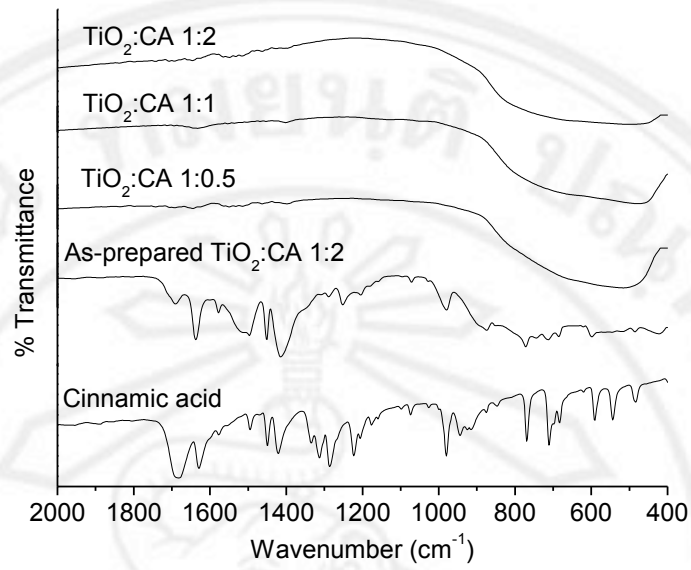
FT-IR spectra of Salicylic acid and as-prepared TiO_2 modified with Salicylic acid (SA) at different mole ratios are shown in Figure 3.10. In the spectrum of SA (Figure 3.10a) the bands are attributed to the stretching and bending coupled C-OH vibrations ($\nu_{\text{C-OH}}$, at 1320-1280 cm^{-1}) [13], the in-plane bending of O-H ($\delta_{\text{O-H}}$, at 1430 cm^{-1}), and the stretching band of the carboxylic acid ($\nu_{\text{C=O}}$, at 1660 cm^{-1}) while the band at 1605 and 1461 cm^{-1} is due to the C-C/C=C stretching vibration of phenyl ring ($\nu_{\text{C=C}}$) [13]. The peak at 450 cm^{-1} was a contribution from the anatase TiO_2 [3]. The peaks of asymmetric (ν_{as} , at 1530 cm^{-1}) and symmetric (ν_{s} , at 1390 cm^{-1}) stretching vibrations due to the splitting of carboxylate groups (COO^-) complexed with surface Ti centers [14] were observed. The value of $\Delta\nu_{\text{a-s}} = 140$ of TiO_2 :SA at different mole ratios implied a bidentate chelating formation between carboxylate anion and surface Ti^{4+} ions. An increasing of mole ratio of TiO_2 :carboxylic acid

resulted in higher peak intensity of carboxylate group due to enhancing the complexed of OH group and carboxylic group (COOH).

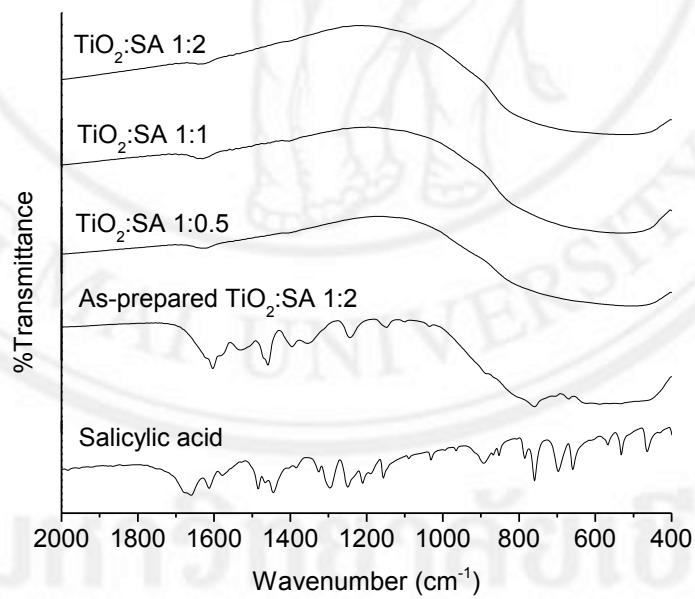
FTIR spectra of TiO_2 :BA, TiO_2 :CA and TiO_2 :SA at different mole ratios calcined at 600 °C for 3h compared with the as-prepared samples and pure carboxylic acids are shown in Figure 3.11 (a-c). After calcination at 600 °C for 3h, the peaks due to carboxylic acid (carboxylate salt, phenyl ring) disappeared. The IR results indicated that trace amount of carboxylic acid was hardly removed and high thermal treatment was required.



a



b



c

Figure 3.11 IR spectra of TiO₂:Carboxylic acid (a) Benzoic acid, (b) Cinnamic acid and (c) Salicylic acid calcined at 600 °C for 3h

3.2.4 Application of photocatalyst

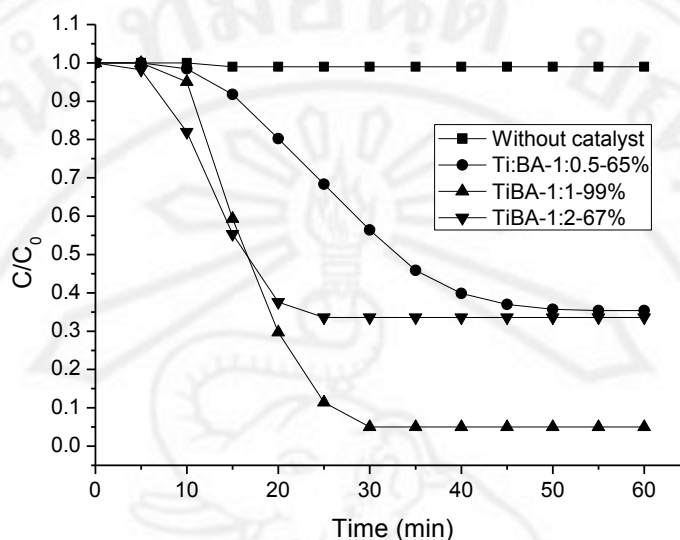


Figure 3.12 Photocatalytic mineralization of phenol under UV light irradiation over $\text{TiO}_2\text{:BA}$ in the mole ratio of 1:0.5 (◆), 1:1 (▲), 1:2 (▼) calcined at 600 °C 3h and without catalyst (■).

Figure 3.12 showed photocatalytic activities of the $\text{TiO}_2\text{:BA}$ mole ratio of 1:0.5, 1:1 and 1:2 calcined at 600 °C evaluated by the mineralization of phenol under UV irradiation. The catalyst suspension (1 g/L) was prepared in deionized water and the suspension pH was adjusted to 7 using 0.1 M NaOH. The initial concentration of phenol was 500 μg carbon. As a comparison, the photolysis of phenol was also carried out at the same condition but without any catalyst. The Photocatalytic degradation was calculated as follows:

$$\text{Photocatalytic degradation \%} = \left(\frac{C_0 - C}{C_0} \right) \times 100 \quad (3.3)$$

where C_0 is the initial concentration and C is the concentration of phenol at different time intervals. The result showed that phenol photolysis is ca. 0.5% which can be

negligible. The TiO₂:BA of 1:1 gave the highest photoactivity of *ca.* 95 % whereas the TiO₂:BA of 1:0.5 and 1:2 provided only *ca.* 65% and 67 % respectively.

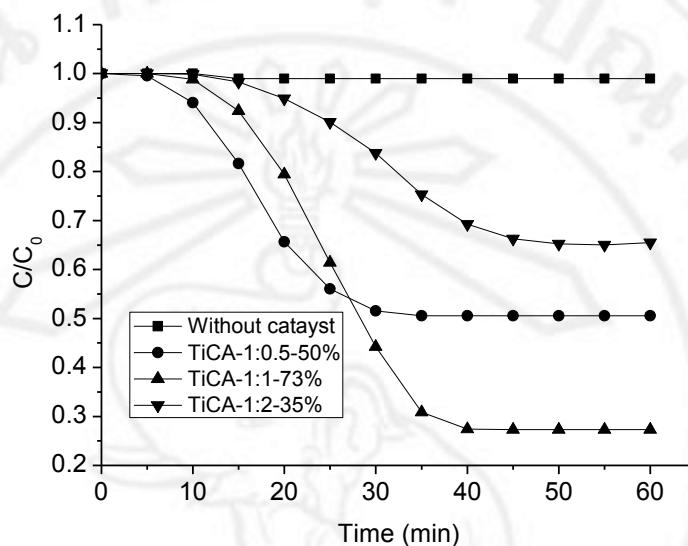


Figure 3.13 Photocatalytic mineralization of phenol under UV light irradiation over TiO₂:CA in the mole ratio of 1:0.5 (◆), 1:1(▲), 1:2 (▼) calcined at 600 °C 3h and without catalyst (■).

The photocatalytic activities of the TiO₂:CA at different mole ratios calcined at 600 °C for 3 h are shown in Figure 3.13. The TiO₂:CA of 1:1 provided the highest photoactivity of *ca.* 73% whereas the TiO₂:CA of 1:0.5 and 1:2 provided only *ca.* 50% and 35 % respectively. Although the TiO₂:CA in 1:2 mole ratio had the highest surface area of 78.2 m²/g, this material did not provide the best photoactivity. Therefore, the surface area is unlikely the main factor affecting the photocatalytic activity observed in this study. Other factors influencing the photocatalyst activities are such as bandgap energy, particle size and crystallinity. Figure 3.14 shows the photocatalytic activities of TiO₂:SA calcined at 600 °C 3h. The results show that

TiO₂:SA 1:0.5 has the highest photoactivity of ca. 83% whereas the TiO₂:SA 1:1 and 1:2 provided only ca. 29% and 42% respectively.

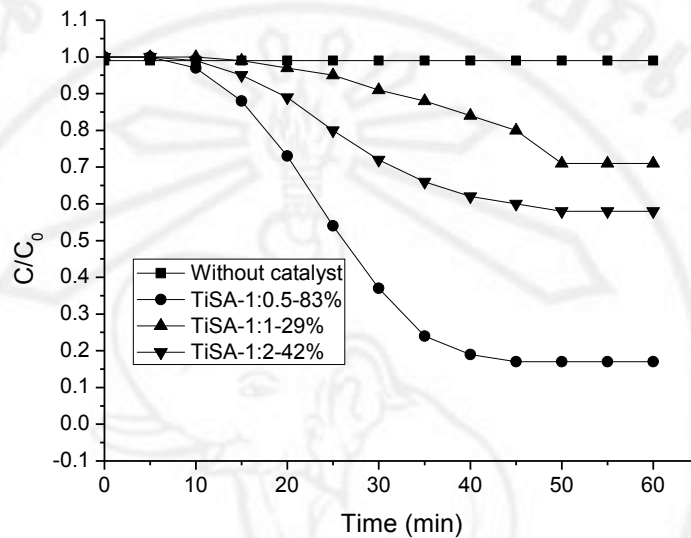


Figure 3.14 Photocatalytic mineralization of phenol under UV light irradiation by TiO₂:SA in the mole ratio of 1:0.5 (◆), 1:1 (▲), 1:2 (▼) and without catalyst (■) calcined at 600 °C 3h.

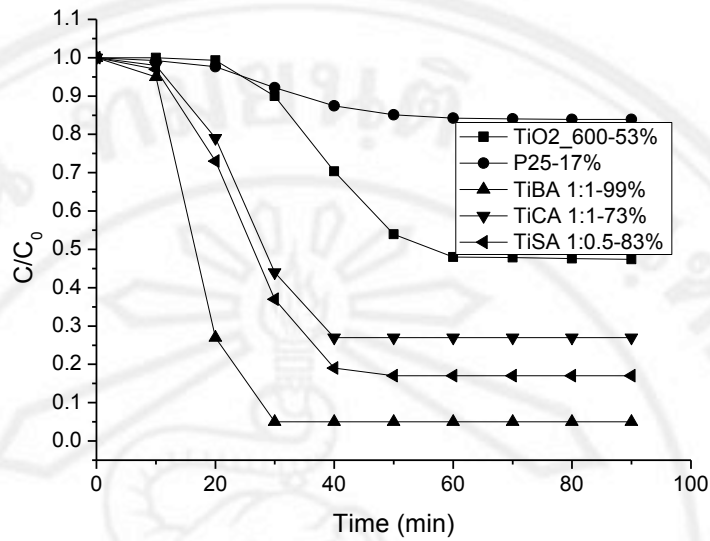


Figure 3.15 Photocatalytic mineralization of phenol under UV light irradiation by TiO₂:BA in 1:1 (▲), TiO₂:CA in 1:1 (▼), TiO₂:SA in 1:0.5 (◆) P25 (●) and TiO₂ 600 oC 3h (■).

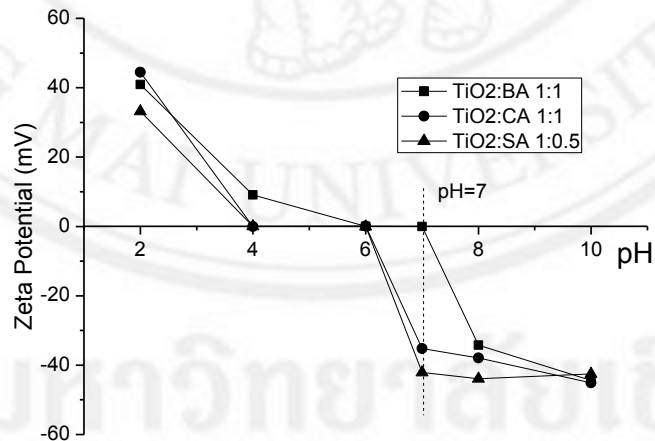
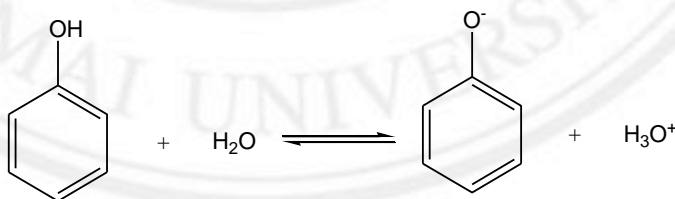


Figure 3.16 Zeta Potential plotted as a function of pH of TiO₂:BA in 1:1 (■), TiO₂:CA in 1:1 (●) and TiO₂:SA in 1:0.5 (▲)

Figure 3.15 showed the comparison among the best TiO₂:Carboxylic acid photocatalyst, the commercial P25 TiO₂ and pure TiO₂. The results clearly demonstrated the superior performances of the TiO₂:BA 1:1 compared with those samples, possibly because of Ti:BA 1:1 has high surface area (Table 3.2) and has less negative charge on surface. The zeta potential plotted as a function of pH of TiO₂:BA 1:1, TiO₂:CA 1:1 and TiO₂:SA 1:0.5 showed in figure 3.16. Those efficiencies can be explained on the basis of the zero point charge of TiO₂ [15]. The zero point charge is known as the pH value at which the concentration of protonated and deprotonated surface groups are equal. The pH for the zero point charge (pzc) of acid-modified TiO₂ is 6, the following equilibrium reactions being operated [16]:



where TiOH is the titanol surface group.



Scheme 2. Dissociation of phenol in water solution [17]

At a pH 3 the molecule of phenol is non-dissociated (neutral) and the surface of TiO₂ also possessed a positive charge (TiOH₂⁺) according to the equation 3.4. Addition, when the pH is adjusted with perchloric acid (HClO₄), the ClO₄⁻ anions [18] (equation 3.6) are also adsorbed at the surface of TiOH₂⁺ [19] resulting in the competitive adsorption between the anions and phenol molecule. At pH 10, the pKa

of phenol is 9.95 [20]. The phenoxide ion is formed and stabilised to some extent due to the delocalization of the negative charge on the oxygen atom around the ring, so at this high pH value the position of equilibrium lies well to the right [17] (Scheme 2). Since the surface charge of all acid-modified TiO_2 is negative (TiO^-) according to equation 3.5, the electrostatic repulsion between the negative surface of TiO_2 and the phenoxide ion (phenol^-) might be present. In addition, the presence of the electrostatic repulsion also reduces the adsorption of phenol, thus decreasing the phenol degradation efficiency [17]. In our study at pH 7, the surface charge of $\text{TiO}_2:\text{BA}$ 1:1 was neutral whereas those of $\text{TiO}_2:\text{SA}$ 1:0.5 and $\text{TiO}_2:\text{CA}$ were negative, therefore the lowest repulsion interaction between the catalyst surface and phenol would occur in the case of $\text{TiO}_2:\text{BA}$ 1:1 catalyst compared with those of $\text{TiO}_2:\text{SA}$ 1:0.5 and $\text{TiO}_2:\text{CA}$, hence the highest photocatalytic activity.

REFERENCES

1. Simakov, S. A.; Tsur, Y., Surface stabilization of nano-sized titanium dioxide: improving the colloidal stability and the sintering morphology. *Journal of Nanoparticle Research* **2007**, 9 (3), 403-417.
2. Behnajady, M.; Eskandarloo, H.; Modirshahla, N.; Shokri, M., Investigation of the effect of sol-gel synthesis variables on structural and photocatalytic properties of TiO₂ nanoparticles. *Desalination* **2011**, 278 (1), 10-17.
3. Xiao, J.; Peng, T.; Li, R.; Peng, Z.; Yan, C., Preparation, phase transformation and photocatalytic activities of cerium-doped mesoporous titania nanoparticles. *Journal of Solid State Chemistry* **2006**, 179 (4), 1161-1170.
4. Ryczkowski, J., IR spectroscopy in catalysis. *Catalysis Today* **2001**, 68 (4), 263-381.
5. Ito, S.; Inoue, S.; Kawada, H.; Hara, M.; Iwasaki, M.; Tada, H., Low-Temperature Synthesis of Nanometer-Sized Crystalline TiO₂ Particles and Their Photoinduced Decomposition of Formic Acid. *Journal of colloid and interface science* **1999**, 216 (1), 59-64.
6. Sirita, J.; Phanichphant, S.; Meunier, F. C., Quantitative analysis of adsorbate concentrations by diffuse reflectance FT-IR. *Analytical chemistry* **2007**, 79 (10), 3912-3918.
7. Singh, J., *Optical properties of condensed matter and applications*. John Wiley & Sons: **2006**; Vol. 6.

8. Peled, A., *Photo-excited processes, diagnostics and applications: fundamentals and advanced topics*. Springer: **2003**.
9. López, R.; Gómez, R., Band-gap energy estimation from diffuse reflectance measurements on sol–gel and commercial TiO₂: a comparative study. *Journal of sol-gel science and technology* **2012**, *61* (1), 1-7.
10. Viriya-Empikul, N.; Sano, N.; Kikuchi, T.; Bureekaew, S.; Tanthapanichakoon, W.; Charinpanitkul, T., Hydrothermal synthesis of titanate nanostructures with high UV absorption characteristics. *Journal of Industrial and Engineering Chemistry* **2010**, *16* (1), 63-67.
11. Rajeshwar, K.; de Tacconi, N. R.; Chenthamarakshan, C., Semiconductor-based composite materials: preparation, properties, and performance. *Chemistry of Materials* **2001**, *13* (9), 2765-2782.
12. Jiang, B.; Yin, H.; Jiang, T.; Yan, J.; Fan, Z.; Li, C.; Wu, J.; Wada, Y., Size-controlled synthesis of anatase TiO₂ nanoparticles by carboxylic acid group-containing organics. *Materials chemistry and physics* **2005**, *92* (2), 595-599.
13. Qu, Q.; Geng, H.; Peng, R.; Cui, Q.; Gu, X.; Li, F.; Wang, M., Chemically Binding Carboxylic Acids onto TiO₂ Nanoparticles with Adjustable Coverage by Solvothermal Strategy. *Langmuir* **2010**, *26* (12), 9539-9546.
14. Nara, M.; Torii, H.; Tasumi, M., Correlation between the vibrational frequencies of the carboxylate group and the types of its coordination to a metal ion: an ab initio molecular orbital study. *The Journal of Physical Chemistry* **1996**, *100* (51), 19812-19817.

15. Madhu, G.; Raj, M.; Pai, K. V. K.; Rao, S., Photodegradation of methylene blue dye using UV/BaTiO₃, UV/H₂O₂ and UV/H₂O₂/BaTiO₃ oxidation processes. *Indian journal of chemical technology* **2007**, *14* (2), 139-144.
16. Lam, S.-M.; Sin, J.-C.; Mohamed, A. R., Parameter effect on photocatalytic degradation of phenol using TiO₂-P25/activated carbon (AC). *Korean Journal of Chemical Engineering* **2010**, *27* (4), 1109-1116.
17. <http://www.chemguide.co.uk/organicprops/phenol/acidity.html>. (15 July 2013)
18. Covington, A.; Tait, M.; Wynne-Jones, W., Dissociation of Perchloric Acid in Aqueous Solution at 25 °C. *Proceedings of the Royal Society of London. Series A. Mathematical and Physical Sciences* **1965**, *286* (1405), 235-250.
19. Bekkouche, S.; Bouhelassa, M.; Salah, N. H.; Meghlaoui, F., Study of adsorption of phenol on titanium oxide (TiO₂). *Desalination* **2004**, *166*, 355-362.
20. http://en.wikipedia.org/wiki/Phenol#Phenoxide_anion. (15 July 2013)
21. Daneshvar, N.; Salari, D.; Niaei, A.; Rasoulifard, M.; Khataee, A., Immobilization of TiO₂ nanopowder on glass beads for the photocatalytic decolorization of an azo dye CI Direct Red 23. *Journal of Environmental Science and Health, Part A* **2005**, *40* (8), 1605-1617.